Additive Manufacture of Refractory Alloy C103 for Propulsion Applications

Omar R. Mireles[1] and Omar Rodriguez[2]
NASA Marshall Space Flight Center, Huntsville, AL, 35812, USA

Youping Gao[3]
Castheon Inc., Thousand Oaks, CA, 91320, USA

Noah Philips[4]
ATI Specialty Alloys, Albany, OR, 97321, USA

C103 is niobium alloy used in high temperature operating environments. Traditional manufacture methods suffer from feedstock constraints, difficult to machine, high buy-to-fly ratios, and high costs resulting in a limited number of suppliers. Additive manufacture (AM) offers advantages in production of complex parts, improved properties, reproducibility, with significant material cost and schedule savings. The objectives of this project was to investigate the feasibility to AM C103, develop powder feedstock, optimize process parameters, establish design criteria, investigate post-process heat treatments, and determine material properties. AM C103 proved feasible, increased design flexibility, improved mechanical properties compared to wrought, and resulted in an order of magnitude cost reduction.

I. Nomenclature

AM	=	additive manufacture
BCC	=	body-centered cubic
BO	=	beam offset
D	=	hatch spacing
D10	=	diameter at which 10% of the population lie below
D50	=	diameter at which 50% of the population lie below
D90	=	diameter at which 90% of the population lie below
E	=	modulus of elasticity
E_a	=	area energy distribution
EBSD	=	electron back-scatter diffraction
EDM	=	electro-discharge machining
EDS	=	energy dispersive spectroscopy
FCC	=	face-centered cubic
HCF	=	high cycle fatigue
HIP	=	hot isostatic press
HRB	=	hardness Rockwell B
IPF	=	inverse pole figure
IQ	=	image quality
L-PBF	=	laser powder bed fusion

[1] Additive Manufacture R&D Engineer, In-Space Propulsion Branch.
[2] Materials Engineer, Materials Characterization Branch.
[3] CEO.
[4] Principal Research Metallurgist, Materials Research.

MPa = mega-Pascal
MSFC = Marshall Space Flight Center
P = power
PSD = particle size distribution
PSU = Portland State University
RCS = reaction control system
Sa = surface roughness (arithmetic mean)
SEM = scanning electron microscopy
SR = stress relief
t = layer thickness
TEM = transmission electron microscopy
UTS = ultimate tensile strength
v = laser scan speed
XRD = x-ray diffraction
YS = yield strength
Z = build direction
ε = strain
μm = micrometer
wt% = weight percent
%TD = percent theoretical density

II. Introduction

NASA Marshall Space Flight Center (MSFC) is leveraging Additive Manufacturing (AM) methodologies for of propulsion applications. AM shows great potential to generate complex and optimized components from an array of materials while decreasing cost and lead time when compared to traditional methods. One area of development is the implementation of refractory materials for green propulsion, reaction control systems (RCS), and radiative cooled nozzles. C103 (Nb-10Hf-1Ti) is solid-solution strengthened niobium alloy used in aerospace applications in sustained high temperature operating environments, particularly in propulsion systems where regenerative cooling is not available. Near net shaping has been traditionally produced through forging and machining. Commercially available C103 bar stock with has a maximum diameter of 114 mm (4.5 in). Larger sizes suffer from insufficient prior work and larger and/or non-uniform grain size causing the material to fails to meet ASTM B655. Such feedstock size limits significantly limits design options. Although C103 is Machin able by conventional subtractive process, it is difficult to machine and when combined with sophisticated geometries result in high buy-to-fly ratios, high costs, and limited number of suppliers. Cost and schedule can also be impacted by larger forging sizes and small part counts. Laser Powder Bed Fusion (L-PBF) AM offers advantages in production of complex monolithic parts not attainable through conventional methods, reproducibility, significant material and cost savings, and a greater degree of schedule control. In addition, L-PBF AM can produce fine geometric features with a superior surface finish when compared to other AM processes. AM addresses conventional manufacture limitations that make C103 competitive within the aerospace market.

III. Methodology

The objectives of this study are to investigate the feasibility to AM C103, optimize process parameters, establish design criteria, investigate post-process heat treatments, and determine material properties to enable the AM C103 for propulsion applications.

A. Powder Production and Characterization

C103 powder were produced and underwent characterization to determine particle size distribution (PSD), morphology, density, and chemistry. Scanning electron microscopy (SEM) was used to observe a spherical morphology and density was determined to be greater than 99.9 %TD. PSD and circularity was measured using a Malvern Morphologi G3 optical analyzer at MSFC. PSD analysis gave a D10 of 12.6 μm, D50 (median) of 33.8 μm, and D90 of 49.1 μm with a median circularity of 0.98 (highly spherical). As with pure Nb the powder crystalized in the β phase. Chemistry was in accordance with ASTM B625 except for oxygen, with a maximum allowable content of 600 ppm for sufficient passivation to allow for safe handling. AM grade C103 powder is reactive and shipped as metal powder hazard class 4.1.

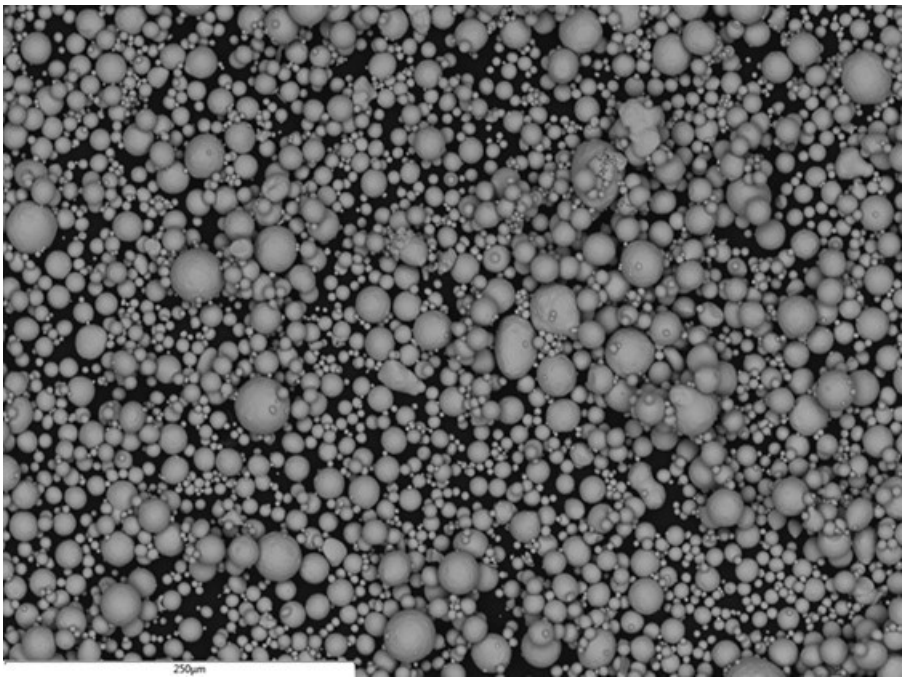

Fig. 1 SEM micrograph of C103 L-PBF AM powder.

B. L-PBF Build Parameter Development

A design of experiments was conducted to identify starting build parameters to include laser power (*P*), laser speed (*v*), hatch distance (*D*), and layer thickness (*t*). Castheon conducted parameter development on a GE Concept Laser M2. Parameters are optimized with the use of optical microscopy with the intent of minimizing porosity with a lower selection criteria of >99.5 %RD. Results from parameter development trails were used to identify an optimized set of parameters that have sufficient build speed yet with a sufficiently low volumetric energy density to minimize residual stress induced geometric distortion. Volumetric energy density (J/mm^3) is used for the core or infill scan strategy, which is determined using (1).

$$E_v = \frac{P}{vDt} \tag{1}$$

P is units of W, *v* in mm/s, *D* in mm, and *t* in mm. Parameters vary for each machine to due nominal laser focus diameter, which is 80 µm for the M2 with melt pool diameter of 1.8 to 2.5 times the laser focus diameter. The support structure and contour scan strategy are single line scans, where the area energy density as is determined by (2).

$$E_a = \frac{P}{vt} \tag{2}$$

Geometry specific parameters such as beam offset (BO) and design constraints such as maximum unsupported overhanging surface angle were determined. The maximum unsupported overhang surface varies between 40-45° from the build direction (*Z*) with a low to moderate amount of residual stress induced distortion, much like IN625. Metallographic and mechanical specimens will be produced using the optimized parameters. In order to investigate the orientation-dependent variation microstructure, tensile, and compression specimens were printed at different orientations with respect to *Z*.

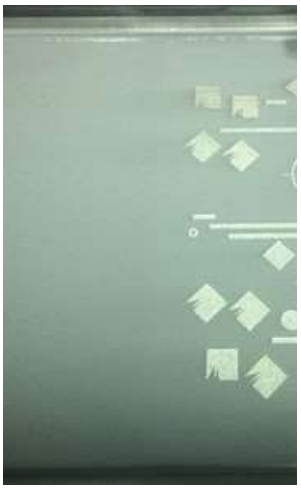

Fig. 2 C103 specimen printing on the Castheon GE Concept Laser M2.

C. Post-Process Heat Treatments

Vacuum Stress Relief (SR) and Hot Isostatic Press (HIP) heat treatment schedules were identified in the literature with the cycles conducted at NASA MSFC. Specimens underwent powder removal, sonication in isopropyl alcohol (99%) for 30 minutes, compressed air dried, stored in a desiccator for 24 hours, and then wrapped in tantalum sheet. Since Nb-base alloys are extremely oxygen sensitive it is critical to wrap them in more sensitive Ta sheet in order to serve as a sacrificial oxygen trap, thus preserving the components from excessive oxidation that may result during heat treatment. AM C103 specimens underwent SR heat treatment at 1100 °C in a vacuum of 10^{-4} torr for 1 hour then furnace cooled to room temperature before removal.

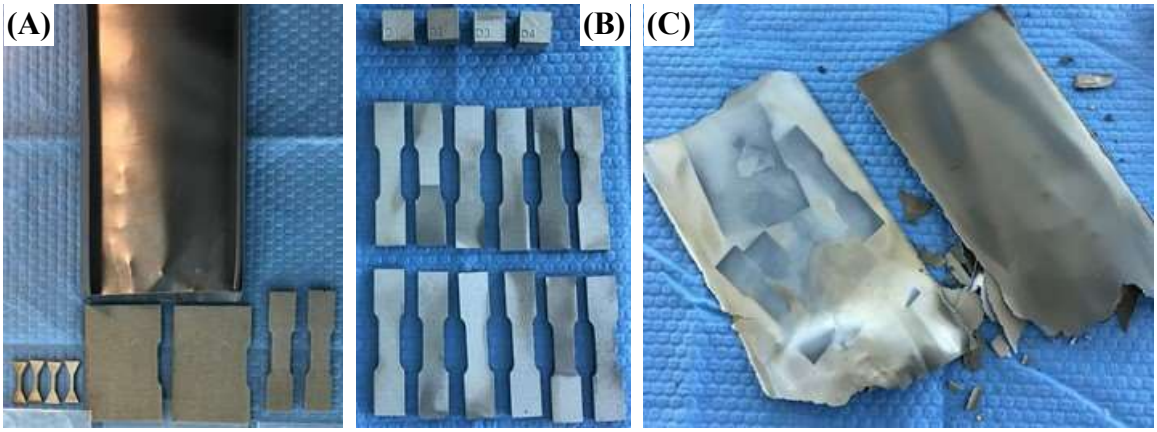

Fig. 3 Specimens & Ta wrap pre-stress relief (A), specimens post-SR & HIP (B), post-SR and HIP Ta wrap brittle from C and O absorption (C).

D. Microstructural Characterization

As-built, SR, and SR+HIP condition specimens underwent metallographic preparation and evaluation in order to characterize the evolution of the microstructure with respect to material condition. Optical micrograph analysis in the in the XZ plane reveal sufficient overlap between adjacent melt pools and minimal porosity as shown in Figure 4A and 4B. Porosity image analysis determined the as-built density of 99.986 %TD and a SR+HIP density of 99.993 %TD, which is above the target threshold of 99.95 %TD. Optical micrographs of the XY plane show the scan rotation strategy, which for a Concept Laser platform is a rotation of 90° between layers as illustrated in Figures 4C and 4D. As is typical of the L-PBF process, the microstructure exhibits a refined grain size distribution in XY with elongated grains in the Z direction. The grain size of AM C103 does not grow substantially between the as-built to the SR+HIP conditions, although there partial conversion indicating incipient recrystallization. Lack of grain growth as a function of heat treatment is unexpected since refractory metals are notorious for rapid grain growth at elevated temperature.

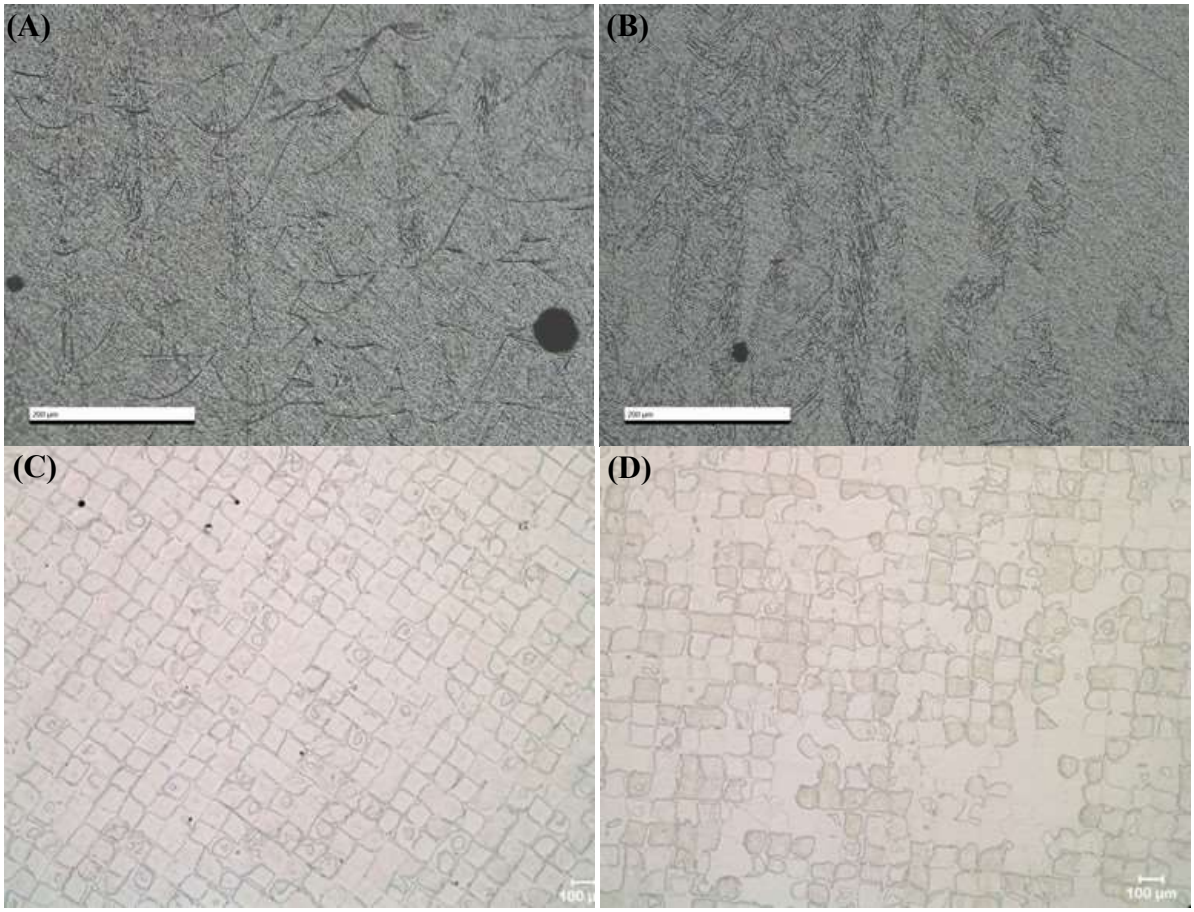

Fig. 4 Optical micrograph at 500x in the XZ plane in the as-built (A) and SR+HIP (B) conditions. Optical micrographs in the XY plane in the as-built (C) and SR+HIP conditions (D).

Retention of the refined microstructure of AM is in sharp contrast to the significant grain growth that occurs between wrought specimens in the as-received condition compared to the heat treated condition as illustrated in Figure 5A and 5B. Due to the refined grain structure it can be expected that mechanical properties of AM C103 in the SR+HIP conditions will likely be comparable to or exceed that of wrought C103.

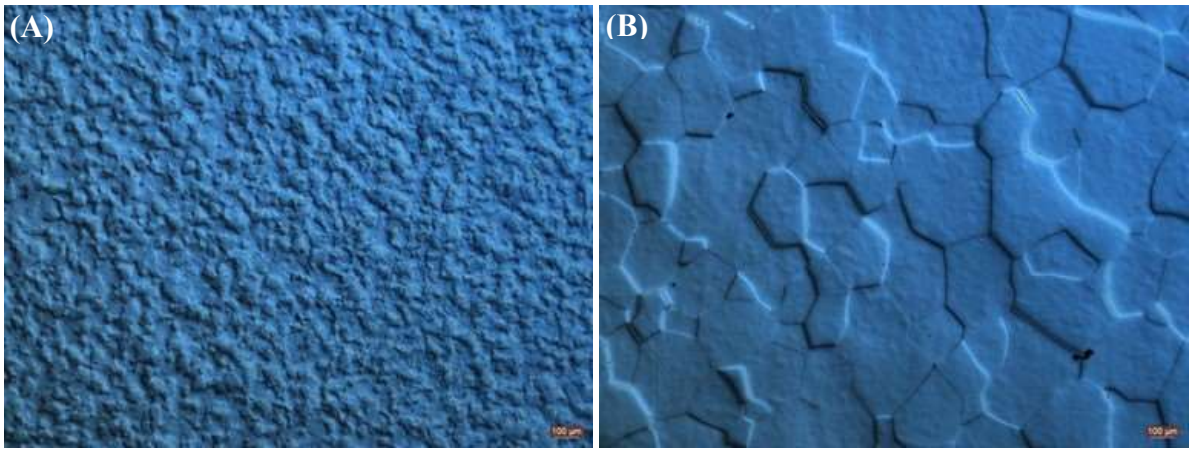

Fig. 5 Polarized optical micrograph of wrought C103 showing substantial grain growth between the as-received (A) and heat treated conditions (B).

Low magnification Scanning Electron Microscope (SEM) micrographs show as-built specimens with minor porosity situated primarily along the grain boundaries, which is typical for L-PBF microstructures. Heat treated specimens also revel sufficient melt pool overlap with the same spatial porosity distributions, along grain boundaries, as seen in the as-built condition. Energy dispersive x-ray spectroscopy (EDS) elemental analysis reveal the qualitative primary elemental constituents for C103 of Nb, Hf, and Ti with no additional peaks indicating a lack of elemental contamination of either the as-built or SR+HIP conditions.

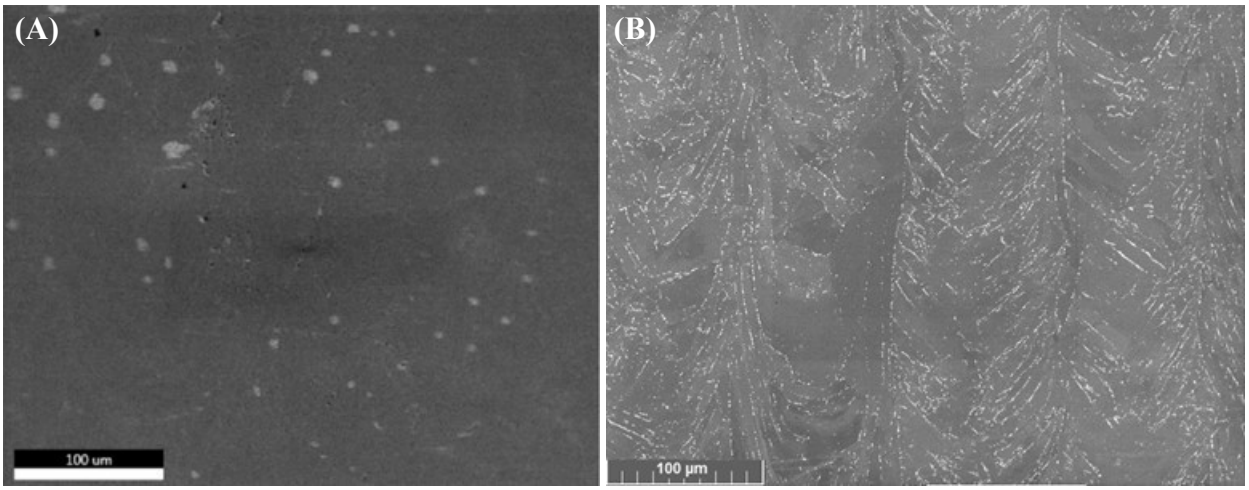

Fig. 6 SEM micrographs at 500x in the XZ plane: as-built (A) and SR+HIP (B).

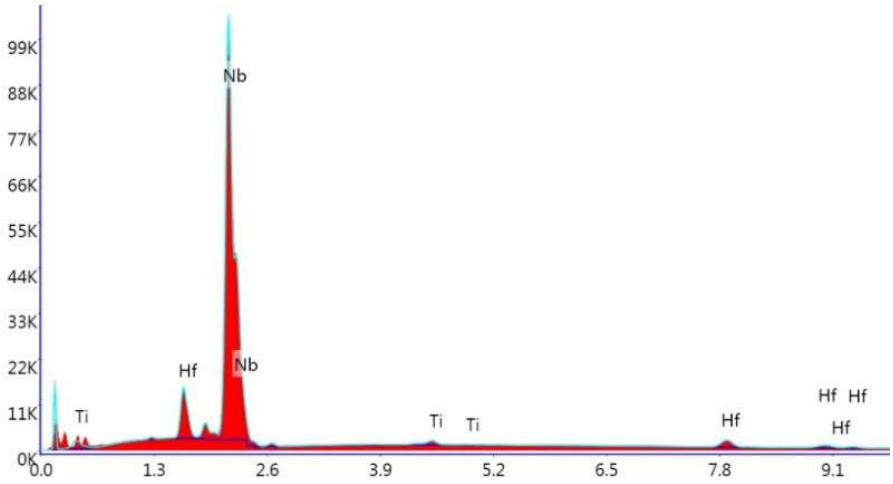

Fig. 7 AM C103 EDS spectra in the as-built condition with no change in the heat treatment.

In order to determine the grain size, orientation, and phase distribution Electron backscatter diffraction (EBSD) was utilized to generate Inverse Pole Figure (IPF+IQ) images as shown in Figures 7A and Figure 8A. The EBSD IPF images in the XZ plane reveal the typical as-built AM microstructure of dendritic grain growth parallel to the build direction with adjacent melt pool overlap. Phase maps were generated as shown in Figures 8B and Figure 9B. Nb being the primary elemental constituent of C103 results in a near-homogeneous BCC crystal structure, which is depicted in the phase map images as the blue phase. The phase maps also shows trace amounts of an FCC phase shown in red. It is possible that the trace FCC phases are precipitates that formed during the solidification process as they are present in the as-built condition phase maps. The trace quantities of the FCC phase tends to decrease with the SR and HIP heat treatment, which could be indicative of phase dissolution. In order to better understand the spatial distribution and character of potential secondary phases additional analytical methods are required and will be discussed later in the study.

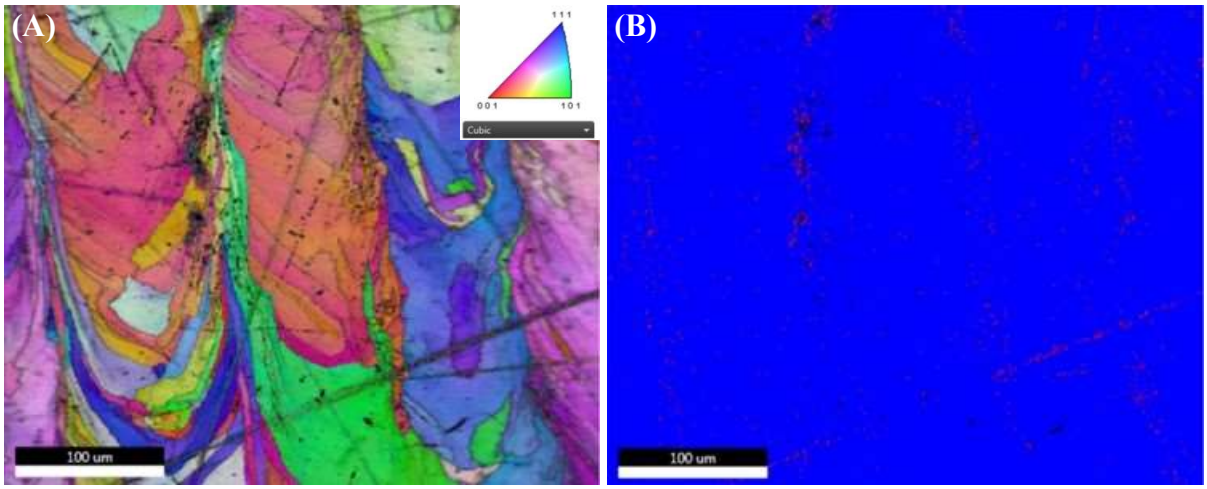

Fig. 8 EBSD IPF of as-built grain in the XZ plane (A). Phase image with 99% BCC and 1% FCC (B).

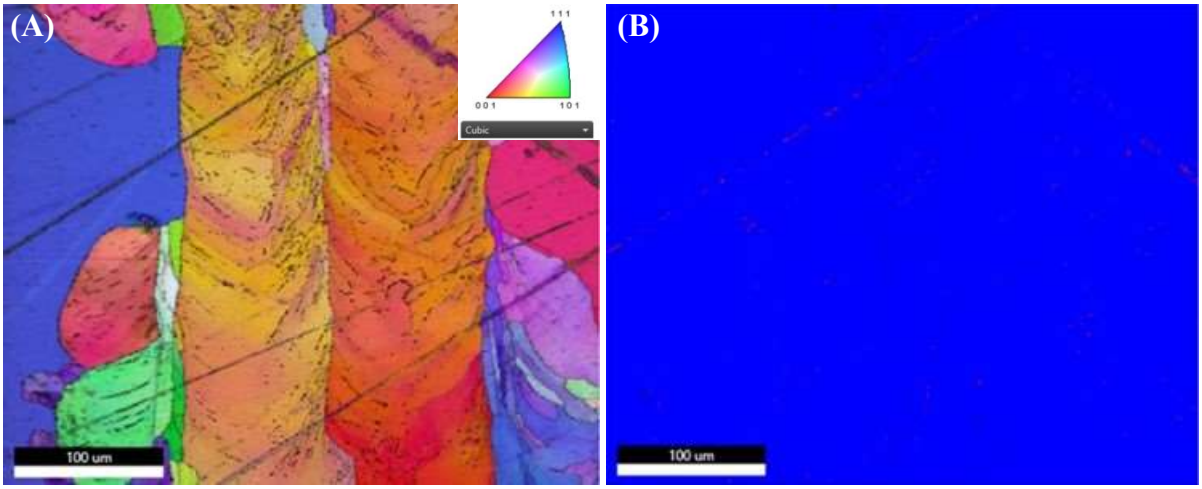

Fig. 9 EBSD IPF of SR+HIP in the XZ plane (A). Phase image 99% BCC and 1% FCC (B).

Grain size as a function of condition was characterized using image intercept methods. The as-built average grain size was determined to be 19.6 µm with a standard deviation of 24.7 µm, with a slight amount of grain growth in the SR+HIP condition with average grain size of 36.3 µm and standard deviation of 34.2 µm.

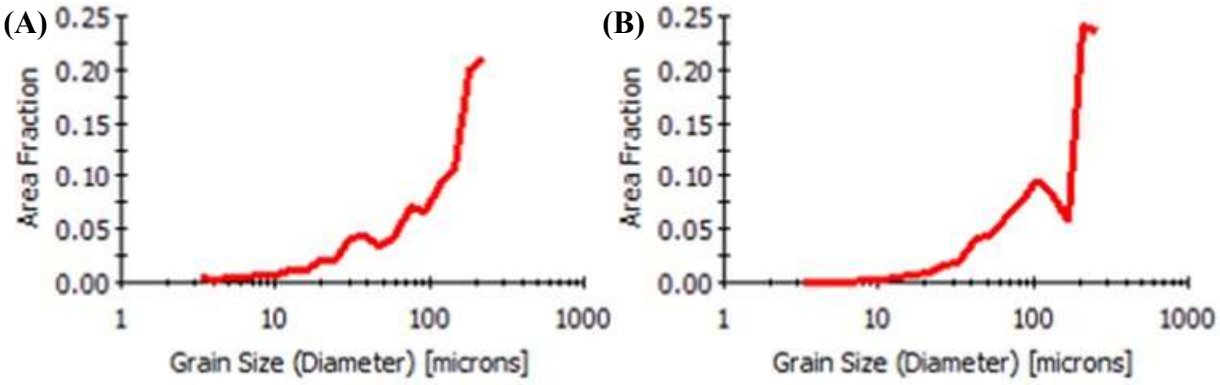

Fig. 10 Grain size distribution of as-built (A) and SR+HIP (B) conditions.

Investigation into the nature of the 1% FCC identified in the as-built EBSD phase map as well as potential secondary precipitates formed during heat treatment was conducted though Transmission Electron Microscopy (TEM). Specimens were prepared with a Focused Ion Beam (FIB)-SEM prior to TEM. TEM micrographs of the as-built and SR+HIP conditions are depicted in Figure 11A through Figure 11D. It can be seen that few precipitates were identified in the as-built condition and correlating EDS data it can be inferred that the secondary phase is likely HfO_2. The micrographs show that the precipitates have a fairly uniform distribution along grain boundaries and but also intra-grain. It can be seen that the precipitate population decreases from the as-built to SR+HIP conditions. The higher magnification TEM micrographs (Figures 11C and 11D) show what appear to be sub-micron pores along grain boundaries. This is an unexpected results as prototypic L-PBF pores along grain boundaries are typically an order of magnitude larger than these pores. Possible explanations for the sub-micron pores along the grain boundaries could be attributed to secondary phases destroyed during heat treatment or perhaps inclusion pull-out during metallographic preparation.

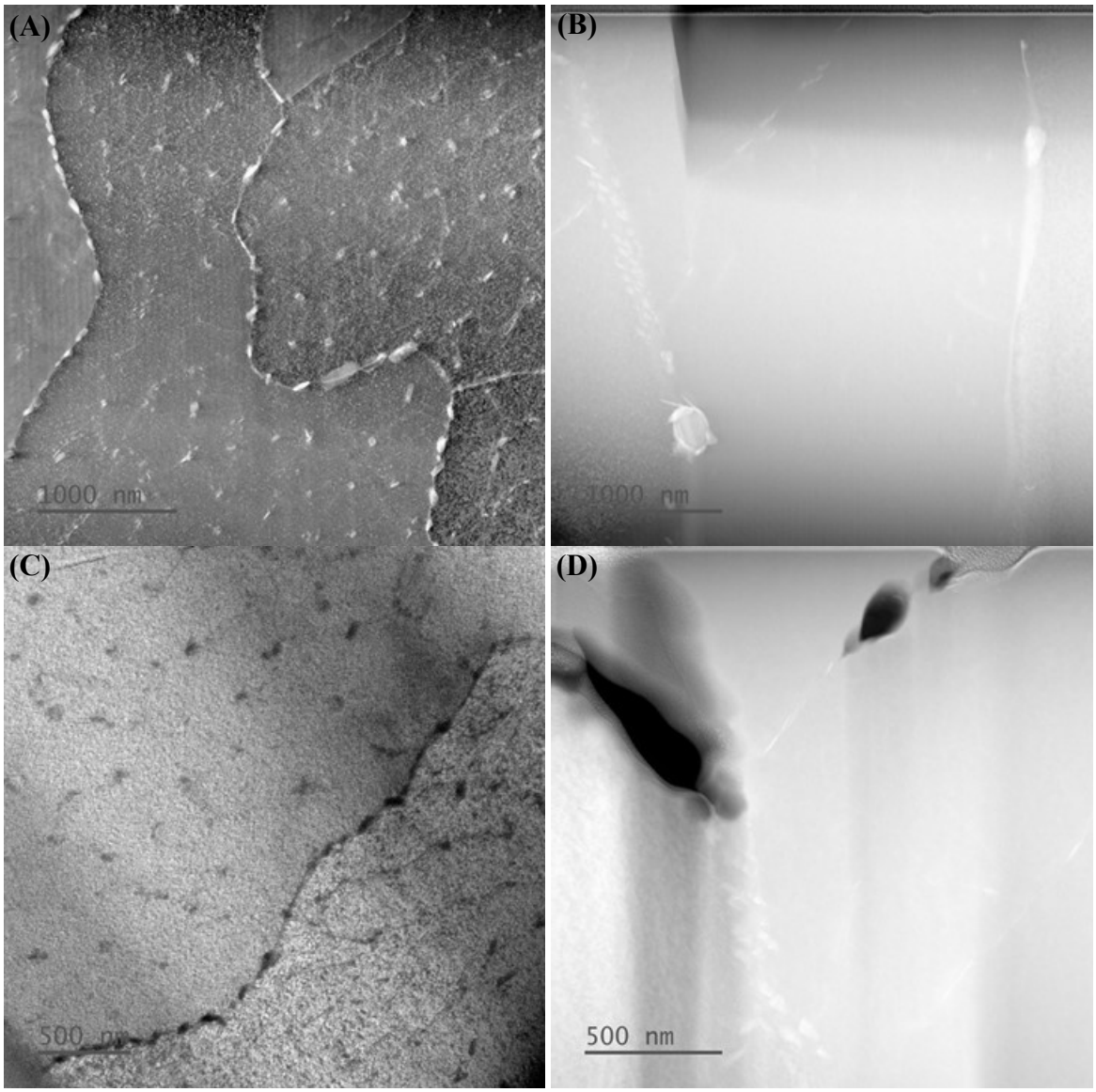

Fig. 11 TEM micrograph in the as-built (A) and SR+HIP conditions (B) showing HfO_2 precipitates. Higher magnification as-built (C) show precipitates and small pores along grain boundaries. SR+HIP (D) show fewer intra-granular precipitates with pores and precipitates along grain boundaries.

Trace element chemical analysis (LECO) was conducted in order to identify potential sources of contamination or compositional changes during the manufacture process; from L-PBF through heat treatment. Trace elemental analysis results shown in Table 1 show that there is oxygen and nitrogen pick-up during AM build process. In addition, there is also small amounts of contamination pick-up during SR and HIP heat treatments; however, these are in the form of surface oxide scales, which can be removed prior to use or subsequent coating operations.

Table 1 LECO trace element chemical analysis.

Condition	O (ppm)	N (ppm)	H (ppm)
Powder	441	26	4
As-built	TBD	TBD	TBD
SR+HIP	1070	150	5

E. Powder Reuse

As with any AM powder it is advantageous to maximize powder re-use to minimize material loss and cost. However, much like other oxygen sensitive alloys, such as Ti6Al4V-Grade23 the number of re-use cycles is limited not only by PSD and morphology but elemental chemistry. Powder with excessive of dissolved oxygen can induce inter-layer oxide deposits, resulting in poor inter-layer bonding and adversely impact mechanical properties [3]. Powder oxygen levels can increase with reuse but can be mitigated by sieving under inert atmosphere. If oxygen becomes excessive, reconditioning by oxygen removal is possible either by vacuum heat treatment with low flow H_2, or through an RF plasma spherodizer also by adding a small amount of H_2 to the argon. These methods have been identified in the publically available literature but were not verified during this effort. It is recommended that the number of powder re-use cycles and reconditioning methods be characterized to maximize useful feedstock life.

F. Surface Roughness Characterization

As-built surface roughness (Sa) as a function of geometric angle was measured on a number of specimens using a Keyence VR-3200 wide area 3D scanner using a magnification of 80x in super-fine mode. Surface finish was found to be typical for L-PBF, taking into account the layer thickness, laser focus diameter, and powder PSD. Table 3 shows the resulting surface finish measures as a function of angle from the build direction (Z). Additional surface finish improvement is readily achievable using commercially available surface modification methods such as shot peen, chemical etch, slurry hone, and electro-polish. Future tasks will need to thoroughly evaluate the applicability of these surface modification methods and combined processes to AM C103 in order to determine the impact of surface finish on the fatigue properties and adherence of protective coatings such as R512E [2].

Table 3 AM C103 Surface Roughness

Angle (°)	Sa (µm)
0	12.9
45	8.1
90	10.5

G. Mechanical Property Evaluation

A series of mechanical tests were performed in order to characterize the behavior of AM C103. The complete specimen test matrix is illustrated in Table 2. Specimens were tested to determine mechanical properties as a function of material condition and temperature. MSFC conducted room temperature quasi-static ($0.001\ \varepsilon^{-1}$) behavior of tensile specimens using a Psylotech meso-scale load frame equipped with a 10kN load cell. Specimens were tested with its loading axis parallel to the build direction Z. Deformation was recorded by the crosshead displacement. The engineering stress and strain of the loaded lattice specimens were obtained by dividing the reaction force by the original cross-sectional area and the displacement by the un-deformed height of the specimens respectively.

Table 2 Mechanical Property Test Matrix.

Test type	Temp	Build Orientation	Condition	Qty	Total	Data
Tensile	21 °C (70 °F)	x-y	AM As-built	2	8	Full stress-strain curve to failure
		x-y	AM SR	1		
		x-y	AM HIP	1		
		z	AM As-built	2		
		z	AM SR	1		
		z	AM HIP	1		
	1093 °C (2000 °F)	x-y	AM As-built	2	8	UTS, total elongation
		x-y	AM SR	1		
		x-y	AM HIP	1		
		z	AM As-built	2		
		z	AM SR	1		
		z	AM HIP	1		
Gleeble Compression	21 °C (70 °F)	z	AM As-built	2	7	Compressive strength up to yield point, converted to tensile yield strength.
		z	AM SR	1		
		z	AM HIP	1		
		n/a	Wrought	1		
		n/a	Wrought SR	1		
		n/a	Wrought HIP	1		
	1093 °C (2000 °F)	z	AM As-built	2	7	
		z	AM SR	1		
		z	AM HIP	1		
		n/a	Wrought	1		
		n/a	Wrought SR	1		
		n/a	Wrought HIP	1		
	1371 °C (2500°F)	z	AM As-built	2	7	
		z	AM SR	1		
		z	AM HIP	1		
		n/a	Wrought	1		
		n/a	Wrought SR	1		
		n/a	Wrought HIP	1		
	1704 °C (3100°F)	z	AM As-built	2	7	
		z	AM SR	1		
		z	AM HIP	1		
		n/a	Wrought	1		
		n/a	Wrought SR	1		
		n/a	Wrought HIP	1		
Density	RT	xyz	AM As-built	4	6	%TD

Room temperature tensile test results show yield strength (YS), ultimate tensile strength (UTS), and strain at failure (ε) for As-Built, SR, and SR+HIP conditions as illustrated in Figure 12. The consolidated results with associated standard deviations are shown in Table 3.

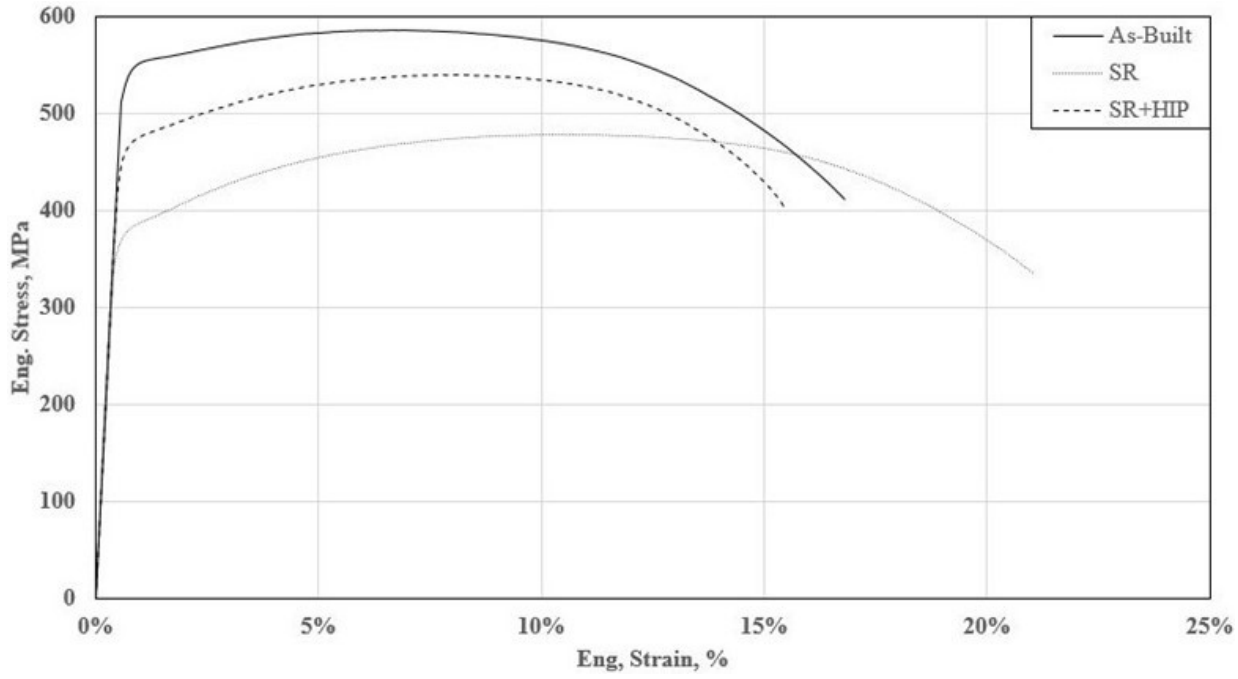

Fig. 12 AM C103 stress-strain curves vs. material condition. Specimens printed in the *Z* direction.

Table 3 AM C103 room temperature tensile properties in the Z direction

Condition	YS_{avg} (MPa)	UTS_{avg} (MPa)	ε_{avg} (%)
As-Built (Z)	560.43±1.47	410.94±0.12	16.67±0.2
SR (Z)	410.5±0.28	334.9±1.02	20.79±0.4
SR+HIP (Z)	452.46±60.35	326.03±106	18.88±4.83

SR decreases YS and UTS while increasing ε, which would be consistent with annealed behavior. SR+HIP results in an increase in YS and UTS with decreasing ε; however, the data exhibited unusually high variation and is likely attributed to a low specimen count and potential for build induced variation.

Tensile tests at temperatures up to 1200 °C were conducted by Westmoreland. Compression tests at temperatures up to 1700 °C were conducted at the Portland State University (PSU) using a Gleeble 3500. Tests were conducted in an argon after numerous evacuation and fill cycles. Ambient and elevated temperature mechanical property test results of L-PBF specimens in the SR+HIP condition are compared to specification requirements and wrought results. Room temperature YS and UTS of L-PBF SR+HIP condition exceed wrought, while elongation is lower. UTS at 1093 °C of L-PBF in all three conditions is higher than wrought. The high strength is likely attributed to the small grain size and possibly fine distributed oxides from the L-PBF process that act as a strengthener and stabilizer [1].

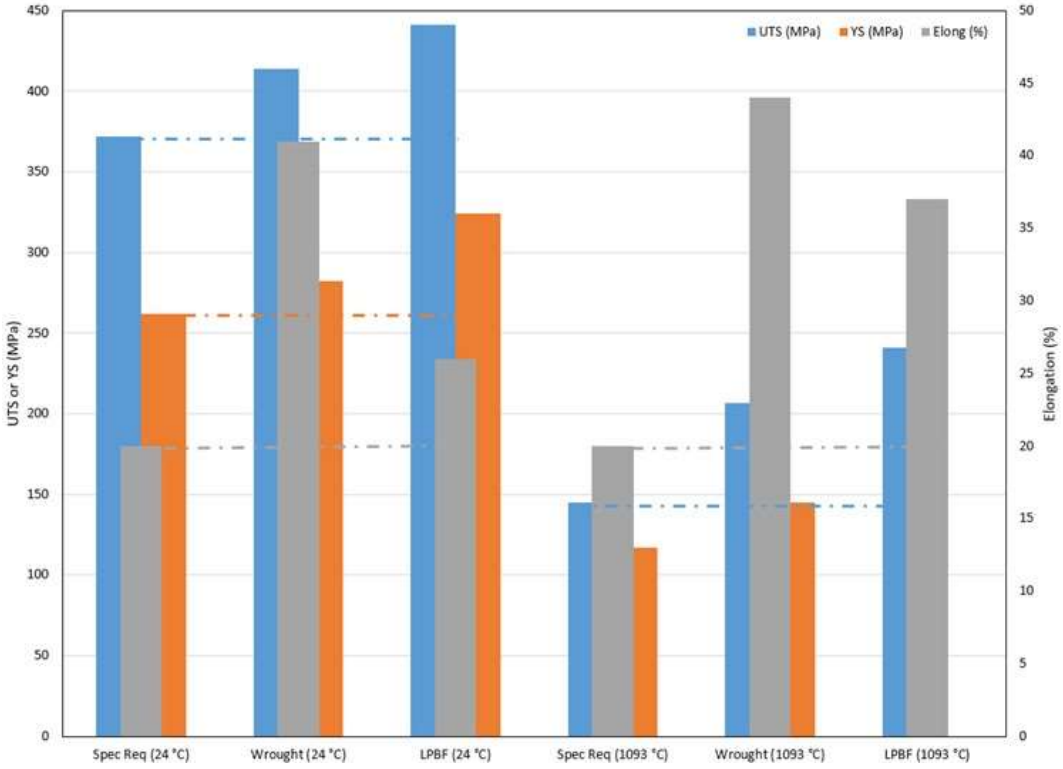

Fig. 13 C103 ambient and elevated temperature mechanical property comparison.

Micro-indentation test results shown in Table 4 exhibit loss of hardness between the as-built and SR+HIP conditions, which is expected and is in accordance with elongation data as a function of heat treatment.

Table 4 AM C103 Hardness

Condition	Hardness (HRB)
As-built	93
SR+HIP	83

H. Cost Comparison

Traditional C103 component manufacture is expensive due to the high cost of the feedstock in addition to machining, heat treatment, and waste disposal. Minimum order quantities for most wrought alloys industry-wide start at approximately 45 kg (100 lb.) and the cost per unit mass varies depending on vendor, customer use rate, raw material rates, etc. Since C103 is primarily used in thrusters, throat sections, and small main propulsion systems the parts tend to be thin walled converging/diverging geometries. Arriving at these shapes can result in 95-98% of the bar stock machined away, or a 20:1 to 50:1 buy-to-fly ratio. Assuming a 20:1 buy-to-fly ratio, the cost of a part in feedstock alone is 5% and 95% in machining waste, not including machining time or machining waste disposal, which is proportional to machining mass. C103 is considered relatively difficult to machine, resulting in a limited number of machine shops with the requisite experience to meet aerospace GD&T specifications. Ultimately, a machined C103 part can cost several thousand dollars but the waste can be several tens of thousands of dollars.

AM C103 powder (L-PBF specification) is approximately 33% more expensive than the average cost of wrought feedstock. Thus, to generate the same part via AM as machined the feedstock cost is approximately 33% more, not including print time, heat treatment, final machining, and waste disposal (powder and machining). However, unlike machining, AM allows for the desired near-net shape to be produced with minimal machining. AM waste is typically 5-10% of the printed part mass resulting from over-sized powder, support structures, and sacrificial geometric features at interfaces to be machined away to meet surface finish requirements. Consequently, the AM buy-to-fly ratio is approximately 1.1:1. In addition, the vast majority of AM powder is reused for additional builds as long as fresh powder is gradually added and that morphology and chemistry remain within feedstock specifications. Therefore, like a machined part, an AM part will also cost several thousand dollars; however, unlike traditional manufacture the waste will cost a few hundred dollars not tens of thousands of dollars. The difference in feedstock costs alone to arrive at an equivalent part constitute an order of magnitude cost reduction by using AM. The cost savings, reproducibility, schedule control, and properties of AM C103 have significant aerospace industry implications for broad implementation of an alloy that may have been previously avoided due to the aforementioned constraints. AM C103 is now readily available to be utilized into high temperature service applications such as RCS thrusters, Green Propulsion chambers, lander main propulsion systems, hypersonic wing leading edge surfaces, etc.

Fig. 14 NASA MSFC AM C103 Green Propulsion Thruster and Stand-off.

IV. Conclusion

AM C103 has been proven feasible and greatly increases design flexibility by eliminating bar stock size constraint limitations. The fast solidification rate from L-PBF process prevents micro-segregation, meaning even large components will be compliant with ASTM B655 and the resulting small grain size distribution improves UTS and YS when compared to wrought properties. A series of successful hot fire tests of AM C103 thrusters were conducted but details are beyond the scope of this study. The Test Readiness Level of AM C103 was increased from 3 to 5 and AM has enabled C103 components to be produced at an order of magnitude cost reduction in the price of materials alone when compared to traditional manufacture processes. Potential follow-on activities should evaluate surface finish modification impact on the deposition process of protective silicide coatings, such as R512E onto AM C103 substrates [2]. A hot fire test campaign for green propulsion, RSC, and in-space propulsion is required to drive TRL higher and

adoption to flight. In addition, x-ray computer tomography (CT) will be unsuitable for inspection of parts since it will be unable to resolve defects due to a poor signal-to-noise ratio since refractory alloys are made from high atomic number elements, which are essentially radio opaque [4], [5]. Alternative non-destructive evaluation methods will be to be investigated for use on AM refractory alloys.

Acknowledgments

The authors would like to thank Marvin Barnes, Richard Booth, Daniel Cavender, Sarah Rengifo, Pat Salvail, Jason Turpin, and Craig Wood of NASA MSFC; Sanghamitra Deb, Richard Martens, and Gregory Thompson of the University of Alabama Central Analytical Facility; Bill Wood and Graham Tewksbury of PSU; and Jeff Powell of Westmoreland. This project was funded under NASA Cooperative Agreement Notice #80MSFC18N0001.

References

[1] Lambert, J.B., *Refractory Metals and Alloys, Properties and Selection: Nonferrous Alloys and Special-Purpose Materials*, Vol. 2, ASM Handbook, ASM International, 1990, pg. 557-558.
[2] Levine, S.R., and Merutka, J.P., "*Performance of Coated Columbium and Tantalum Alloys in Plasma Arc Reentry Simulation Tests*," NASA T/N D-7617, 1974.
[3] Kaczmarek, I., et al., "*Tantalum (Ta) and Niobium (Nb) Containing Alloy Powders for Application in Additive Manufacture,*" Proceedings of the Additive Manufacture with Powder Metallurgy Conference, 2019.
[4] Turner, J., *Atoms, Radiation, and Radiation Protection*, John Wiley & Sons Inc, New York, NY, 1995, pp. 187-192.
[5] Knoll, G. F., *Radiation Detection and Measurement* – 3th ed., John Wiley and Sons Inc., New York, NY, 1999, pp. 629-631.